Modeling and Analysis of Wireless Resonant Magnetic Microactuators

Zoltán Nagy, Dominic R. Frutiger, Remco I. Leine, Christoph Glocker, and Bradley J. Nelson

Abstract— We present a dynamic model of the wireless resonant magnetic microactuator (WRMMA), which is a key component of the MagMite family of microrobots. We analyze the interbody force and integrate the nonsmooth and nonlinear equations of motion using a time-stepping integration scheme. We investigate the influence of system parameters, such as friction, the frequency of the applied force, the magnitude of the applied field, the effect of a clamping force, and the effect on velocity when phase shifting the clamping signal with respect to the magnetic signal. Our results are qualitatively consistent with experimental observations, and explain several nonintuitive phenomena. We show that the robots are highly sensitive to the phase of the clamping force, that the velocity can switch directions with changing frequency, and that both erratic and controlled motion occur under specific conditions.

I. INTRODUCTION

Microactuators are of general interest because they allow precise positioning and manipulation at the microscale. They are a prerequisite for powering and enabling biomedical microrobots that have the potential for "noninvasive" procedures, offering less injury and faster patient recovery time in comparison with current laparoscopic techniques. Possible applications of microrobots are delivery and implantation of active structures in the human body, targeted therapy, marking, and biopsy [1].

While many technologies must be developed and synergistically integrated in order to realize such applications, the aspects that need to be addressed first when it comes to wireless mobile microrobotic platforms are power supply and propulsion. These aspects remain challenging to date since both onboard batteries and classical wireless power transmission using, e.g., electromagnetic coupling between coils, are inefficient for microdevices due to scaling effects [2]. As a result, veritable microrobotic systems featuring wirelessly controlled agents with principle dimensions in the submillimeter range have only emerged in recent years [3]–[11].

For effective propulsion at the microscale, methods that convert external energy directly into mechanical motion without any complex mechanisms, e.g., those involving cogs or electronic circuits, are more practical as they lower energy loss and fabrication complexity. As an example, consider the wireless resonant magnetic microactuator (WRMMA) shown in Fig. 1(a) and introduced in [7]. The WRMMA consists of two nickel masses connected through a gold spring and has overall dimensions of $300 \times 300 \times 50\mu m^3$. As shown in Fig. 1(b), one mass—the body—rests on a

Z. Nagy, D. Frutiger and B. Nelson are with the Institute of Robotics and Intelligent Systems, ETH Zurich, Switzerland. R. Leine and C. Glocker are with the Center of Mechanics, ETH Zurich, Switzerland. Z. Nagy is the corresponding author (nagyz@ethz.ch).
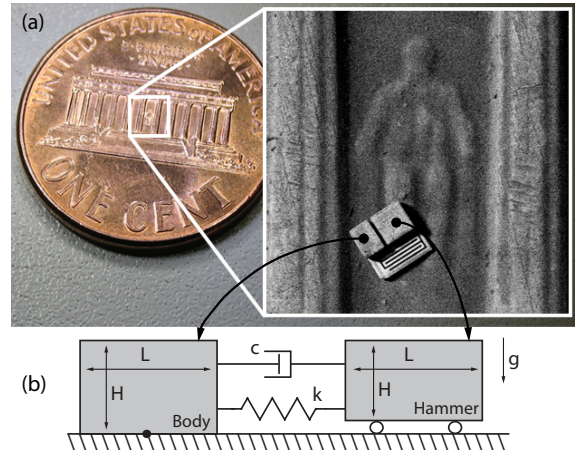
Fig. 1. (a) Wireless resonant magnetic microactuator in size comparison with a US penny. (b) Mechanical model of the WRMMA.

gold support structure which in turn has frictional contact with the substrate, whereas the other one—the hammer—is lifted above the ground and can move freely without friction. Initially not magnetized, the nickel bodies become magnetized when an external magnetic field is applied. As a result, an attractive magnetic force arises between them. Then, time-variant magnetic fields are used to induce oscillatory motion and, it is assumed, impact between the hammer and the body drives the robot forward. An additional electrostatic clamping force between the body and the ground allows arbitrary rectification of the oscillation by effectively controlling the friction between the robot and the ground. Such a device can be used for propelling microrobots—in particular the *MagMites*—a family of microrobotic agents based on the WRMMA, which were introduced in 2007, described in detail in [7], [8], [12] and demonstrated by video [13], [14].

Primary responses and driving behaviors have been experimentally characterized [12], and the overall performance was observed to be largely as intended by design: firstly, reliable turning behavior thanks to alignment with the external magnetic field; and secondly controlled forward and backward motion at near resonance thanks to rectification with a phase-shifted clamping potential in the substrate. Besides these primary behaviors several other modes of operation have been discovered, e.g, naturally driving backwards without the need for a clamping signal. Furthermore, phenomena such as changing the velocity direction when increasing or decreasing the frequency, and also erratic behaviors, were observed.

An analytical or numerical model is necessary in order to understand the observed modes of operation. Several impact actuators have been presented in literature (see [15] and references therein), and analysis of their nonlinear behavior is also available. In general, the analysis is focused on the conditions necessary for impact, and it is implicitly assumed that impact is necessary for motion. However, in [16] it is experimentally observed that the actuator might drive backwards under certain conditions. Yet, the model of the actuator presented in [15] does not address this issue. In fact, most models do not address the influence of external parameters, such as friction or actuation schemes, that are different from a harmonic force. However, in the case of the WRMMA, these parameters have significant influence on the driving performance. For example, with the electrostatic clamping force, the robot can be fixed and released periodically, or an additional variable friction force can be applied.

In this paper, we model and numerically analyze the dynamics of the WRMMA. The simulations are validated with experimental data available for the tethered mode (i.e., when the body is fixed to the substrate) and from the literature. We investigate the influence of the system parameters on the performance, e.g., the velocity, of the robot. That is, we show the influence of friction, and that the direction of motion is reversed with varying frequencies. Finally, we also demonstrate that the velocity of the robot is highly sensitive to the phase of the clamping force.

II. THEORY

The magnetic torque on the WRMMA will act such that the device will align with the applied field. Since rotational inertia scales down faster with size compared with the mass, we assume that the forward motion begins after the WRMMA is aligned with the field. This assumption is well supported by experimental observations. Thus, a 1D model will be employed to describe its motion.

A. Magnetic Interaction

In a homogeneous magnetic field, no net force is exerted on a single, ideally soft, magnetic body. Thus the force between the parts of the WRMMA arises solely due to the interaction of both magnetizations. To estimate this force, we perform a finite element analysis (Maxwell 3Dv12) using a continuous magnetization curve [17], and for fields $B = (1,5)$mT. As shown in Fig. 2, we find that the data can be fit well, the root mean square error being 5.1×10^{-4}N/T^2, to a rational curve of the form

$$F_m(x) = \frac{pB^2}{x^2 + q_1 x + q_2}, \qquad (1)$$

where $q_1 \approx 43.1$µm and $q_2 \approx 201$µm^2 for each B, and p is a constant such that $p/B^2 \approx$ constant.

B. Dynamics

To model the dynamics of the WRMMA, we use the non-smooth dynamics approach as described in [18]–[21]. This approach provides a mathematically sound formalism for the dynamics of rigid bodies with set-valued interaction laws
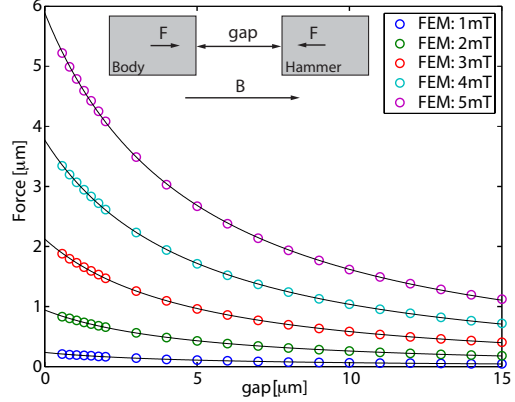

Fig. 2.   Force between the the body and the hammer for different applied fields. The lines represent the best rational fit (see text).

for the description of unilateral contact, friction and impact. Furthermore, Moreau's time-stepping method in combination with a linear complementary problem (LCP) formulation of the contact problem is used for the numerical simulation [19]. Moreau's time-stepping method discretizes the equality of measures

$$\mathbf{M}d\mathbf{u} - \mathbf{h}(\mathbf{q}, \mathbf{u}, t)dt - \sum \mathbf{w}_{Ni}dP_{Ni} - \sum \mathbf{w}_{Ti}dP_{Ti} = \mathbf{0}, \qquad (2)$$

which is a combined description of the nonimpulsive and impulsive motion. Here, dt is the Lebesgue measure on $\mathbb{R}$, $\mathbf{M}$ is the (constant) mass matrix of the mechanical system, $\mathbf{u}$ are the velocities associated with the generalized coordinates $\mathbf{q}$, and $\mathbf{h}$ is the vector of noncontact forces such as spring, damper and gravitational forces. The generalized force directions $\mathbf{w}_{Ni}$, $\mathbf{w}_{Ti}$ and the percussion measures dP_{Ni} and dP_{Ti} describe the contribution of the contact forces/impulses to the dynamics of the system, with the subscripts N and T representing normal and tangential directions and i the contact number. The percussion measure P_i can be decomposed into a nonimpulsive contact force λ_i and the impulsive contact force Λ_i as

$$dP_i = \lambda_i dt + \Lambda_i d\eta, \qquad (3)$$

where $d\eta$ is the atomic differential measure. For more details on this formulation, see [18], [20].

Figure 3 shows the free body diagram of the WRMMA consisting of the body with coordinates (x_1, y_1) and the hammer with coordinate x_2. The generalized coordinates and the associated velocities are

$$\mathbf{q} = \begin{pmatrix} x_1 & y_1 & x_2 \end{pmatrix}^T, \qquad \mathbf{u} = \begin{pmatrix} v_{x,1} & v_{y,1} & v_{x,2} \end{pmatrix}^T \quad (4)$$

with $\dot{\mathbf{q}} = \mathbf{u}$ for almost all t. The system has a frictional contact between the body and the floor with a gap distance given by $g_{N1}(\mathbf{q}) = y_1 - H/2$. We assume that this contact always remains closed, i.e., $g_{N1} = 0$, and, therefore, consider it to be a frictional bilateral contact with sliding velocity $\gamma_{T1}(\mathbf{u}) = v_{x,1}$ and friction coefficient μ. Furthermore, there is a frictionless unilateral contact between the body and the hammer with gap $g_{N2} = x_2 - x_1 - L \geq 0$ and
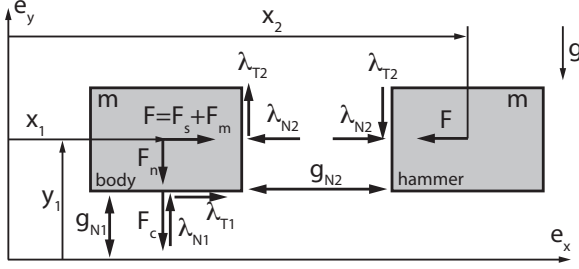
Fig. 3. Free body diagram of the WRMMA.

restitution coefficient ε. The matrices $\mathbf{W}_N = \begin{pmatrix} \mathbf{w}_{N1} & \mathbf{w}_{N2} \end{pmatrix}$ and $\mathbf{W}_T = \begin{pmatrix} \mathbf{w}_{T1} & \mathbf{w}_{T2} \end{pmatrix}$ of generalized force directions are

$$\mathbf{W}_N = \begin{pmatrix} 0 & 1 & 0 \\ -1 & 0 & 1 \end{pmatrix}^T, \qquad \mathbf{W}_T = \begin{pmatrix} 1 & 0 & 0 \\ 0 & 1 & 0 \end{pmatrix}^T. \quad (5)$$

The mass matrix $\mathbf{M} = \operatorname{diag}(m, m, m)$ is constant and the vector $\mathbf{h}$ of the non-contact forces is composed of a normal force $\mathbf{F_n}$, the clamping force $\mathbf{F_c}$ on the body, the spring force $\mathbf{F_s}$, damping $\mathbf{F_d}$ and magnetic force $\mathbf{F_m}$ between the body and the hammer; i.e.,

$$\mathbf{h} = \mathbf{F_n} + \mathbf{F_s} + \mathbf{F_d} + \mathbf{F_m} + \mathbf{F_c}, \quad (6)$$

with

$$\mathbf{F_n} = \begin{pmatrix} 0 & -\beta mg & 0 \end{pmatrix}^T, \quad (7)$$

$$\mathbf{F_s}(g_{N2}) = \begin{pmatrix} -k\Delta g & 0 & k\Delta g \end{pmatrix}^T, \quad (8)$$

$$\mathbf{F_d}(v_{x,1}, v_{x,2}) = \begin{pmatrix} c\Delta v_x & 0 & -c\Delta v_x \end{pmatrix}^T, \quad (9)$$

where the normal force is given in units β of the gravitational force mg to examine the effect of friction, $\Delta g = g_{N2} - g_{N2,0}$ is the elongation of the spring with respect to the equilibrium gap $g_{N2,0} = 15\mu m$, $\Delta v_x = v_{x,2} - v_{x,1}$ is the relative velocity of the bodies, c is the linear damping constant, and

$$\mathbf{F_m}(g_{N2}, t) = \begin{pmatrix} f_m(g_{N2}, t) & 0 & -f_m(g_{N2}, t) \end{pmatrix}^T (10)$$

$$\mathbf{F_c}(t) = \begin{pmatrix} 0 & -f_c(t) & 0 \end{pmatrix}^T. \quad (11)$$

As in the experiments in [12], we set $f_m(g_{N2}, t)$ and $f_c(t)$ as positive square wave functions, i.e., *on/off* signals, with frequency f and their phase being shifted by φ; i.e.,

$$f_m(g_{N2}, t) = \frac{F_m(g_{N2})}{2} \operatorname{sgn}\left(\sin\left(2\pi ft\right)\right) + \frac{F_m(g_{N2})}{2}, \quad (12)$$

$$f_c(t) = \frac{F_c}{2} \operatorname{sgn}\left(\sin\left(2\pi ft + \varphi\right)\right) + \frac{F_c}{2}, \quad (13)$$

where $\operatorname{sgn}(\,\cdot\,)$ is the signum function. For the amplitude of the magnetic force, $F_m(g_2)$, we use (1) with $x = g_{N2}$, and F_c is set such that no motion of the body is observable when clamping is active.

C. Numerical Integration

Following the LCP description from [19], eq. (2) is integrated using a midpoint integration scheme to find the velocity and the position of the both bodies. The main advantage of using this scheme over an event-driven algorithm is its robustness, as it does not require the explicit distinction between the impact, stick and slip phases. In addition, it is easily extendable to problems with even more contacts, i.e., devices with multiple bodies/hammers.

The integration is performed by sweeping over system parameters such as the frequency f. In these parameter sweeps, the initial conditions at a specific frequency are the results of the simulation at the previous frequency. When sweeping the parameters in different directions, this may result in different steady-state solutions—an inherent phenomenon of a nonlinear system. Typically, for each parameter set, we integrate for about 30 periods $T = 1/f$ of the actuation force to allow the system to reach steady-state. Then, for the subsequent 20 periods, the value of the parameter of interest, e.g. the velocity of the robot, at the end of each period is plotted. This results in 20 data points at a specific actuation frequency, and allows for analysis of the periodic response of the system with identification of up to period-20 solutions. Finally, the time-step for the integration dt is set to one thousandth of the actuation period, $dt = 10^{-3}T$, in order to ensure sufficient temporal resolution.

Parameters available from [7] are set as $L = 150\mu m$, $W = 130\mu m$, $H = 50\mu m$, $m = 8.6775 \times 10^{-6} g$, $k = 2\mu N/\mu m$. Experimentally unavailable parameters are fixed for this study as $c = 1 \times 10^{-6} \mu Ns/\mu m$, $\mu = 0.5$ and $\varepsilon = 0.5$.

III. RESULTS

A. Tethered Behavior

It is possible to obtain experimental data for the hammer velocity when the body is fixed to the substrate using a laser doppler vibrometer. In this mode, the WRMMA behaves as a single mass-spring system with undamped natural frequency $f_n = \frac{1}{2\pi}\sqrt{k/m}$, driven by the excitation force (12). In the following, we express the actuation frequency f in units $\tilde{f}$ of the natural frequency, i.e. $f = \tilde{f}f_n$, where, using the parameters from the previous section, we have $f_n = 2416$Hz.

The experimental frequency response of the tethered device from [7] is shown in Fig. 4(a), and the frequency response as predicted by our model in Fig. 4(b). The choice for the applied fields is guided by the available experimental data. We observe good quantitative agreement for low applied fields ($B \le 1.42$mT); for larger fields, our model predicts larger velocities. Possible reasons for this are differences in the geometry (and hence in the forces) due to fabrication variations, and nonlinear and squeeze-film damping. These cause the hammer to impact already at lower velocities. Nevertheless, the impact behavior of the model is in good qualitative agreement with the data, i.e. it plateaus when impact occurs, and is sufficient for our study.

Figure 5 shows the numerically predicted response of the maximal hammer displacement (x_2) for an applied field of $B = 5$mT. We observe that when increasing the frequency, x_2 increases and plateaus almost horizontally, before a fold bifurcation occurs at $\tilde{f} \approx 1.11$ and x_2 drops to the equilibrium gap (15mm). When decreasing the frequencies, hysteresis is observed with, again, a fold bifurcation at $\tilde{f} \approx 1.01$. This behavior is qualitatively consistent with
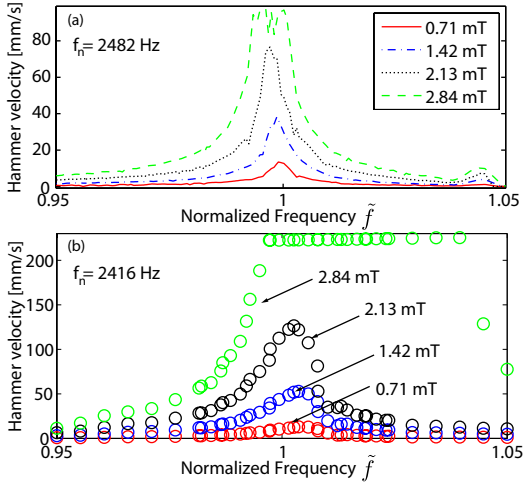
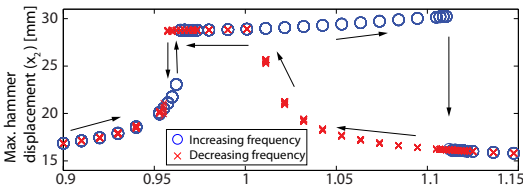Fig. 4. (a) Experimental and (b) numerical frequency response. See text.

Fig. 5. Numerical frequency sweep for the tethered device at $B = 5$mT. Hysteresis is observed at $\tilde{f} = 1.0 - 1.12$.

Fig. 6. (a) Untethered and unclamped ($f_c = 0$) motion is relatively chaotic for low friction. (b) The motion becomes more repeatable at larger friction and a downshift of the actuation frequencies compared with the low-friction case is observable. The time evolution of the motion at the point P is shown in Fig. 7.

results presented in [15], and we conclude that our model adequately predicts the motion of the hammer.

B. Untethered Behavior

The untethered robot behaves as a two-mass oscillator with undamped resonant frequency $\sqrt{2}f_n$. We perform frequency sweeps for different parameter sets and monitor their effects on the mean displacement of the body per actuation period, i.e.,

$$u_{\text{robot}} = \frac{x_1(t + T) - x_1(t)}{T} \qquad (14)$$

For these sweeps, we typically scan roughly the area around the resonant frequency of the untethered device ($\tilde{f} = (0.8, 2)$), and then we increase the resolution of the frequency steps in the interesting areas while decreasing the range of the sweep. The investigated parameters are the strength of the magnetic field $B = \{1, 5\}$mT, the friction $\beta = \{10, 100\}$ and clamping with a phase shift $\varphi = (0, 2\pi)$.

First, we discuss the unclamped mode ($f_c = 0$). For $\beta = 10$, i.e. low friction, the robot can be actuated with frequencies $\tilde{f} = \sqrt{2}$, that is, close to its natural frequency. As shown in Fig. 6(a) we observe chaotic behavior around $\tilde{f} = 1.37$. After the chaotic segment, the device moves with velocities of up to a maximum of about 7mm/s, or about 20 body lengths per second. When the frequency is increased further, the device suddenly stops due to stiction. To overcome this stiction, the driving frequency has to
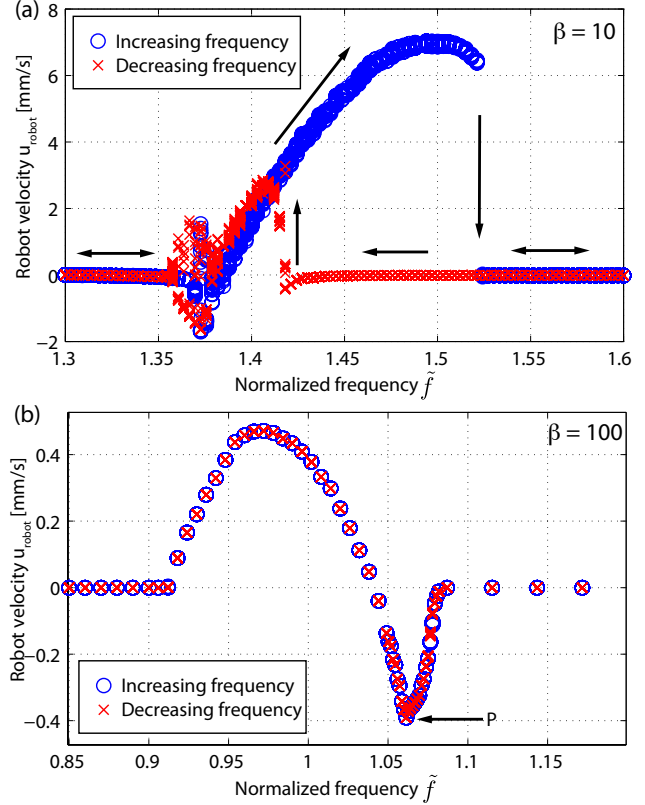
be decreased to $\tilde{f} \approx \sqrt{2}$. This corresponds well with experimental observations [7].

At higher friction, i.e. $\beta = 100$ (still $B = 5$mT), we observe a different behavior, shown in Fig. 6(b). The robot now only moves for actuation frequencies close to $\tilde{f} = 1$. This is due to the large friction that makes the device behave similarly to the tethered case. The motion of this mode seems comparatively regular. In fact, it is interesting that the system exhibits both positive and negative velocities with a sharp transition between them. Since there is no significant hysteresis in the system, this configuration allows bidirectional motion with velocities of about 0.4mm/s by only sweeping the frequency. The lower velocities are intuitively clear: If the friction in the system is large, the robot will move slowly, if at all. On the other hand, the sign change of the velocity—unusual for impact drives—suggests that motion occurs in two manners, i.e., the hammer pushing and pulling the body, and it is not clear if impact occurs at all.

To answer this question, we further examine the motion of both bodies as predicted by the numerical model for the point P in Fig. 6(b), that is $\tilde{f} \approx 1.06$. Figure 7 shows the results for one actuation period T. In Fig. 7(a) we observe two stick-slip phases in the velocity of the body. The examination

reveals that these stick-slip phases are slightly different and thus a net motion in one direction is obtained. In addition, it is clear from Fig. 7(b), where the gap g_{N2} between the bodies is shown, that no impact occurs during this motion as $g_{N2} \neq 0$. Finally, the frequency-dependent velocity change is due to the fact that the stick-slip phases vary depending on the phase of g_{N2} with respect to the magnetic signal (data not shown).

We recall our observation that for low friction, the robot operates around its untethered natural frequency $\tilde{f} = \sqrt{2}$, while for higher friction, the operating frequency is around $\tilde{f} = 1$. This means that the operating frequency in the freely moving mode is an indicator of the friction. Impact drives reported in the literature all operate around their tethered resonant frequency, and thus at high friction; and impact is indeed necessary to overcome the static friction and propel the actuator forward. On the other hand, an upward shift of actuation frequency by a factor of 1.2–1.4 for best performance has been reported when switching from tethered to mobile operation in the case of the MagMites [12]. We conclude that the friction in the system is comparatively small and consequently motion without impact is possible.

We now consider the system with a clamping force (13). Figure 8 shows the significant influence of φ on the system for frequencies $\tilde{f} = 1, 1.1, 1.2$, with $\beta = 10$, and $B = 2.5\text{mT}$. First, we observe that changing φ by approximately π can switch the direction of the velocity—an intended feature of the system. The following effects are revealed by our model: For a specific frequency, the curves may exhibit large changes in the velocity over small changes in φ. For example, for $\tilde{f} = 1.2$, increasing φ from about $\pi/10$ to $\pi/5$ will decrease the velocity from 2mm/s to 0.3mm/s, i.e. almost by a factor 10. We also observe that the curves for the individual frequencies cross. This means that changing frequencies will not always have the same effect. For example, increasing the frequency from $\tilde{f} = 1$ to 1.2 at $\varphi = 0$ will result in an increase in velocity. However, the same frequency increase at $\varphi = \pi/2$ will first increase the velocity, but then the velocity drops to practically zero. This demonstrates the large sensitivity of the system with respect to the phase shift as a reason for the unintuitive behavior of the robots often expressed in sudden changes of the velocity.

Finally, in Fig. 9, we show the performance of the robot when varying the applied field and the friction on the robot for a phase shift $\varphi = \pi$. In 9(a), we see for $B = 2.5\text{mT}$ and $\beta = 10$ that the motion starts in the negative direction for increasing frequencies, and after $\tilde{f} = 0.95$ it becomes positive. The velocity reaches its maximum around 1.2 and then drops suddenly due to stiction. When reversing the frequencies, slight hysteresis is observed. For larger fields (see 9(b)), the device could theoretically be operated in a large frequency range. However, we see chaotic behavior from $\tilde{f} = 1.17$ to 1.27, and at the same time very large velocities. Both effects result in a device that might be difficult to operate. For large fields and large friction, 9(c) shows that the velocity is reduced again and that hysteresis is also much smaller. The device can now be operated in
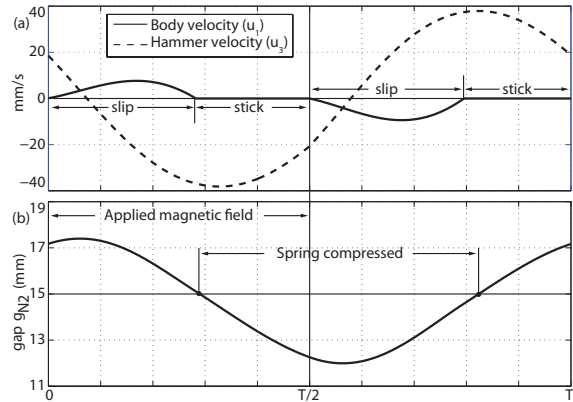

Fig. 7. During one actuation period T ($\tilde{f} = 1.06, B = 5\text{mT}, \beta = 100$): (a) two stick-slip phases occur, and (b) no impact is observable as $g_{N2} \neq 0$.
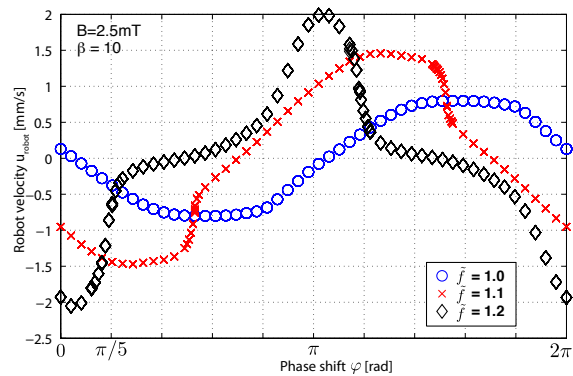

Fig. 8. Influence of the phase shift on the robot velocity.

a band around $\tilde{f} = 1$. Reducing the field now results in a narrower operation band and further decreased velocities (see 9(d). This demonstrates that the model is able to predict a large range of motion patterns that are in good qualitative agreement with experimental observation, i.e. the influence of frequency and friction on the velocity—including segments of chaotic behavior.

IV. SUMMARY AND CONCLUSIONS

We presented a model of the wireless resonant magnetic microactuator.Based on the interbody forces a nonsmooth dynamic analysis was performed to investigate the behavior of the device. We analyzed the influence of various parameters, such as friction and the clamping force. We conclude that the model predicts a large range of motion patterns, which are in good agreement with experimental observations. Specifically, we predict the change in the velocity's direction for increasing frequencies, sudden changes in the velocity due to small variations of the phase shift, and identify relatively low friction as a major source of unintuitive and sometimes chaotic motion. In conclusion, the model can be used to optimize the performance of the system and determine boundaries for the parameters to ensure smooth operation.
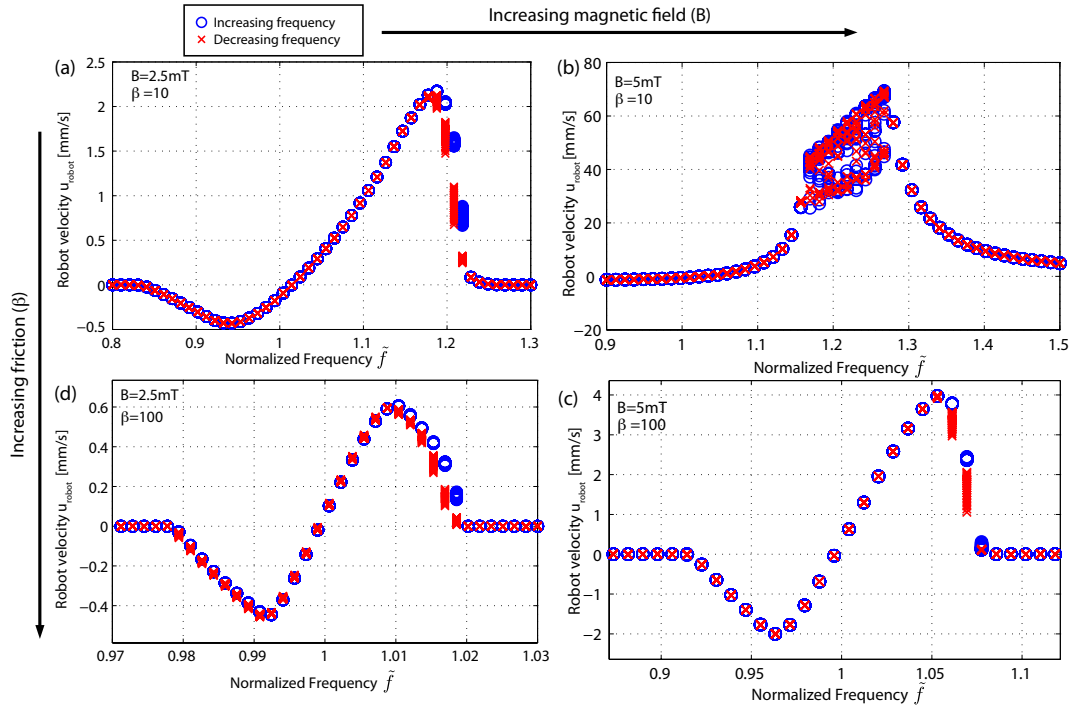
Fig. 9. The influence of the applied field and the friction on the robot actuated with a clamping force with phase shift $\varphi = \pi$. Note the difference in the range on the frequency axes.

V. Acknowledgment

References

[1] B. J. Nelson, I. K. Kaliakatsos, and J. J. Abbott, "Wireless microrobots for minimally invasive medicine," *Annual Review of Biomedical Engineering*, 2010, in press.

[2] J. J. Abbott, Z. Nagy, F. Beyeler, and B. J. Nelson, "Robotics in the small part I: Microrobotics," *IEEE Robotics and Automation Magazine*, vol. 14, no. 2, pp. 92–103, 2007.

[3] A. Yamazaki, M. Sendoh, K. Ishiyama, K. Arai, R. Kato, M. Nakano, and H. Fukunaga, "Wireless micro swimming machine with magnetic thin film," *Journal of Magnetism and Magnetic Materials*, vol. 272, pp. E1741–E1742, 2004.

[4] K. B. Yesin, K. Vollmers, and B. Nelson, "Modeling and control of unthered biomicrorobots in a fluidic environment using electromagnetic fields," *Int. J. Robotics Research*, vol. 25, no. 5-6, pp. 527–536, June 2006.

[5] O. J. Sul, M. R. Falvo, I. R. M. Taylor, S. Washburn, and R. Superfine, "Thermally actuated untethered impact-driven locomotive microdevices," *Applied Physics Letters*, vol. 89, 2006.

[6] B. R. Donald, C. G. Levey, C. D. McGray, I. Paprotny, and D. Rus, "An untethered, electrostatic, globally controllable MEMS micro-robot," *J. of Microelectromech. Systems*, vol. 15, no. 1, pp. 1–15, Feb 2006.

[7] K. Vollmers, D. R. Frutiger, B. E. Kratochvil, and B. J. Nelson, "Wireless resonant magnetic microactuator for untethered mobile microrobots," *Applied Physics Letters*, vol. 92, no. 14, 2008.

[8] D. R. Frutiger, K. Vollmers, B. E. Kratochvil, and B. J. Nelson, "Small, fast, and under control: wireless resonant magnetic micro-agents," in *Proc. Int'l. Symposium on Experimental Robotics*, July 2008.

[9] C. Pawashe, S. Floyd, and M. Sitti, "Modeling and experimental characcerization of an untethered magnetic micro-robot," *Int. J. Robotics Research*, 2009.

[10] L. Zhang, J. J. Abbott, L. X. Dong, B. E. Kratochvil, D. J. Bell, and B. J. Nelson, "Artificial bacterial flagella: Fabrication and magnetic control," *Applied Physics Letters*, vol. 94, no. 6, February 2009.

[11] A. Ghosh and P. Fischer, "Controlled propulsion of artificial magnetic nanostructured propellers," *Nano Letters*, vol. 9, no. 6, pp. 2243–2245, 2009.

[12] D. R. Frutiger, K. Vollmers, B. E. Kratochvil, and B. J. Nelson, "Small, fast, and under control: wireless resonant magnetic micro-agents," *Int. J. Robotics Research*, 2009, invited paper.

[13] D. R. Frutiger, B. E. Kratochvil, K. Vollmers, and B. J. Nelson, "Magmites - wireless resonant magnetic microrobots," in *Proc. IEEE Int. Conf. Robot. Automat.*, May 2008.

[14] D. R. Frutiger, B. E. Kratochvil, and B. J. Nelson, "Magmites - microrobots for wireless micromanipulation under dry and wet conditions," in *Proc. IEEE Int. Conf. Robot. Automat.*, May 2010.

[15] X. Zhao, H. Dankowicz, C. K. Reddy, and A. H. Nayfeh, "Modeling and simulation methodology for impact microactuators," *J. of Micromechanics and Microengineering*, vol. 14, no. 6, pp. 775–784, 2004.

[16] M. Mita, M. Arai, S. Tensaka, D. Kobayashi, and H. Fujita, "A micromachined impact microactuator driven by electrostatic force," *J. Microelectromech. Syst.*, vol. 12, no. 1, pp. 37–41, 2003.

[17] Z. Nagy, O. Ergeneman, J. J. Abbott, M. Hutter, A. M. Hirt, and B. J. Nelson, "Modeling assembled-MEMS microrobots for wireless magnetic control," in *Proc. IEEE Int. Conf. Robot. Automat.*, 2008, pp. 874–879.

[18] C. Glocker, *Set-Valued Force Laws*, ser. Lecture Notes in Applied Mechanics. Springer, 2001, vol. 1.

[19] C. Glocker and C. Studer, "Formulation and preparation for numerical evaluation of linear complementarity systems in dynamics," *Multibody System Dynamics*, vol. 13, no. 4, pp. 447–463, 2005.

[20] R. Leine and H. Nijmeijer, *Dynamics and Bifurcations of Non-Smooth Mechanical Systems*, ser. Lecture Notes in Applied and Computational Mechanics. Springer, 2004, vol. 18.

[21] R. Leine and N. van de Wouw, *Stability and Convergence of Mechanical Systems with Unilateral Constraints*, ser. Lecture Notes in Applied and Computational Mechanics. Springer, 2008, vol. 36.